Spectral Energy Distributions of Companion Galaxies to $z \sim 6$ Quasars

C. Mazzucchelli[1,2,12] , R. Decarli[3] , E. P. Farina[4] , E. Bañados[1] , B. P. Venemans[1] , M. A. Strauss[5] , F. Walter[1,6,7] , M. Neeleman[1] , F. Bertoldi[8] , X. Fan[9] , D. Riechers[10] , H.-W. Rix[1] , and R. Wang[11]

[1] Max-Planck-Institut für Astronomie, Königstuhl 17, D-69117 Heidelberg, Germany
[2] European Southern Observatory, Alonso de Cordova 3107, Vitacura, Region Metropolitana, Chile
[3] INAF—Osservatorio di Astrofisica e Scienza dello Spazio, via Gobetti 93/3, I-40129, Bologna, Italy
[4] Max-Planck-Institut für Astrophysik, Karl-Schwarzschild-Str. 1, D-85748 Garching, Germany
[5] Department of Astrophysical Sciences, Princeton University, Princeton, NJ 08544, USA
[6] National Radio Astronomy Observatory, Pete V. Domenici Array Institute Science Center, P.O. Box O, Socorro, NM 87801, USA
[7] Astronomy Department, California Institute of Technology, MC249-17, Pasadena, CA 91125, USA
[8] Argelander Institute for Astronomy, University of Bonn, Auf dem Hügel 71, D-53121 Bonn, Germany
[9] Steward Observatory, University of Arizona, 933 N. Cherry Street, Tucson, AZ 85721, USA
[10] Cornell University, 220 Space Sciences Building, Ithaca, NY 14853, USA
[11] Kavli Institute of Astronomy and Astrophysics at Peking University, 5 Yiheyuan Road, Haidian District, Beijing 100871, People's Republic of China

Abstract

Massive, quiescent galaxies are already observed at redshift $z \sim 4$, i.e., $\sim$1.5 Gyr after the big bang. Current models predict them to be formed via massive, gas-rich mergers at $z > 6$. Recent ALMA observations of the cool gas and dust in $z \gtrsim 6$ quasars have discovered [C II]- and far-infrared-bright galaxies adjacent to several quasars. In this work, we present sensitive imaging and spectroscopic follow-up observations, with *HST*/WFC3, *Spitzer*/IRAC, VLT/MUSE, Magellan/FIRE, and LBT/LUCI-MODS, of ALMA-detected, dust-rich companion galaxies of four quasars at $z \gtrsim 6$, specifically acquired to probe their stellar content and unobscured star formation rate. Three companion galaxies do not show significant emission in the observed optical/IR wavelength range. The photometric limits suggest that these galaxies are highly dust-enshrouded, with unobscured star formation rates $\mathrm{SFR_{UV}} <$ few $M_\odot \, \mathrm{yr}^{-1}$, and a stellar content of $M_* < 10^{10} \, M_\odot \, \mathrm{yr}^{-1}$. However, the companion to PJ167−13 shows bright rest-frame UV emission (F140W AB = 25.48). Its spectral energy distribution resembles that of a star-forming galaxy with a total SFR $\sim 50 \, M_\odot \, \mathrm{yr}^{-1}$ and $M_* \sim 9 \times 10^9 \, M_\odot$. All the companion sources are consistent with residing on the galaxy main sequence at $z \sim 6$. Additional, deeper data from future facilities, such as the *James Webb Space Telescope*, are needed in order to characterize these gas-rich sources in the first gigayear of cosmic history.

Key words: cosmology: observations – early universe – galaxies: high-redshift – quasars: general

1. Introduction

A large population of massive ($\sim 10^{11} \, M_\odot$), quiescent, and compact galaxies has been observed at very early cosmic times ($2 < z < 4$) when the universe was between $\sim$1.6 and $\sim$3.6 Gyr old (e.g., van Dokkum et al. 2008; Straatman et al. 2014). Several studies suggest that these galaxies formed from gas-rich, major mergers at $3 \lesssim z \lesssim 7$ (e.g., Hopkins et al. 2008; Wuyts et al. 2010). High-redshift ($z \gtrsim 3$) submillimeter galaxies (SMGs) have been invoked as possible progenitors of these massive $z \gtrsim 2$ "red-and-dead" sources (e.g., Toft et al. 2014).

SMGs are galaxies with large infrared luminosities ($L_{\mathrm{IR}} \gtrsim 10^{12} \, M_\odot$), which are thought to experience short and intense episodes of star formation (e.g., Blain et al. 2002; Spilker et al. 2014). Recent studies show that SMGs at $z \sim 3.5$ often have subcomponents or companions when observed at kiloparsec-scale resolution (e.g., Hodge et al. 2013b; Gomez-Guijarro et al. 2018), or located in dense environments (e.g., Hodge et al. 2013a; Riechers et al. 2014), suggesting that these sources have experienced recent mergers. At even higher redshifts ($z \gtrsim 6$), only a few SMGs not hosting a central active galactic nucleus have been observed. Riechers et al. (2013) found a dust-obscured, extremely star-forming SMG at $z = 6.3$ with a star formation rate SFR $\sim 3000 \, M_\odot \, \mathrm{yr}^{-1}$; Fudamoto et al. (2017) and Zavala et al. (2018) discovered a $z = 6.03$ galaxy whose SFR was somewhat smaller ($\sim 950 \, M_\odot \, \mathrm{yr}^{-1}$); Marrone et al. (2018) discovered a pair

of massive SMGs with similar SFR at $z \sim 6.9$. The only other highly star-forming ($\gtrsim 100 \, M_\odot \, \mathrm{yr}^{-1}$) objects known thus far at such redshifts, with luminosities extending to slightly fainter values ($L_{\mathrm{IR}} \sim$ few $10^{11} \, L_\odot$) than classical SMGs, are the host galaxies of $z \gtrsim 6$ quasars (e.g., Walter et al. 2009; Venemans et al. 2012, 2018; Wang et al. 2013; Decarli et al. 2018).

Quasars are among the most luminous sources in the universe; in recent years, the number of such objects known at $z \gtrsim 6$ greatly increased, thanks to the advent of deep, large-area sky surveys (e.g., Fan et al. 2006; Bañados et al. 2016, 2018, Mazzucchelli et al. 2017b; Reed et al. 2017, 2019; Matsuoka et al. 2018; Wang et al. 2018). Observations of the stellar light from their host galaxies have been very challenging, due to the much brighter, nonthermal radiation from the central engine (e.g., Decarli et al. 2012; Mechtley et al. 2012). On the other hand, emission from cool gas and dust in the observed (sub)millimeter wavelength regime has been studied in several sources, providing a wealth of information on the composition, dynamics and conditions in the interstellar medium (ISM) of their hosts (e.g., Maiolino et al. 2009; Willott et al. 2015; Venemans et al. 2016, 2017). In particular, the singly ionized 158 μm carbon emission line, [C II], is one of the main coolants of the ISM and is very bright (it can emit up to 1% of the total far-infrared emission in star-forming galaxies). It has been used extensively as a key diagnostic of galactic physics (see Carilli & Walter 2013 and Diaz-Santos et al. 2017 for reviews, and Herrera-Camus et al. 2018a, 2018b for recent works).

Table 1
Coordinates, Redshifts, Spatial Projected Distances, and Velocity Shifts of the Quasars and the Adjacent Galaxies Studied in This Work

Name	R.A. (J2000)	Decl. (J2000)	z	z_{err}	$\Delta r_{projected}$ (kpc)	$\Delta v_{line\ of\ sight}$ (km s^{-1})	References
SDSS J0842+1218	08:42:29.43	12:18:50.4	6.0760	0.0006			(1)
SDSS J0842+1218c	08:42:28.95	12:18:55.1	6.0656	0.0007	47.7 ± 0.8	−443	(1)
PSO J167.6415−13.4960	11:10:33.98	−13:29:45.6	6.5154	0.0003			(2)
PSO J167.6415−13.4960c	11:10:34.03	−13:29:46.3	6.5119	0.0003	5.0	−140	(2)
PSO J231.6576−20.8335	15:26:37.84	−20:50:00.8	6.58651	0.00017			(1)
PSO J231.6576−20.8335c	15:26:37.87	−20:50:02.3	6.5900	0.0008	8.4 ± 0.6	+137	(1)
CFHQS J2100−1715	21:00:54.70	−17:15:21.9	6.0806	0.0011			(1)
CFHQS J2100−1715c	21:00:55.45	−17:15:21.7	6.0796	0.0008	60.7 ± 0.7	−41	(1)

Note. These measurements are obtained from the narrow [C II] emission line and underlying dust continuum observed by ALMA. References are as follows: (1) Decarli et al. (2017), (2) Neeleman et al. (2019).

Recently, Decarli et al. (2018) and Venemans et al. (2018) undertook a survey of [C II] and underlying dust continuum emission in 27 quasar host galaxies at $z \gtrsim 6$, with the Atacama Large Millimeter Array (ALMA), at a resolution of $1''$, i.e., ~ 5.5 pkpc at those redshifts. Surprisingly, they serendipitously discovered [C II]- and far-infrared-bright companion galaxies in the fields of four quasars, with projected separations of $\lesssim 60$ kpc and line-of-sight velocity shifts of $\lesssim 450$ km s^{-1} (Decarli et al. 2017). In addition, Willott et al. (2017) used ALMA observations at $0''\!.7$ resolution (i.e., ~ 4 pkpc at $z \sim 6.5$) to find a very close companion galaxy to the quasar PSO J167.6415−13.4960 at $z \sim 6.5$, at a projected distance of only 5 kpc and velocity separation of ~ 300 km s^{-1}. Similar sources have also been observed in lower-redshift systems (e.g., at $z \sim 5$; Trakhtenbrot et al. 2017). These findings, together with the discovery of a couple of galaxies adjacent to two quasars at $z \sim 4$ and 6 (McGreer et al. 2014), a Lyα-emitting galaxy ~ 12 kpc away from a $z \sim 6.6$ quasar (Farina et al. 2017), and a close quasar-galaxy pair at $z \sim 6$ (Neeleman et al. 2019), provide observational support to the theoretical paradigm that $z \sim 6$ quasars reside in rich galactic environments (e.g., Volonteri & Rees 2006; Overzier et al. 2009; Angulo et al. 2012). However, we note that other studies did not find overdensities of [C II]/dust-continuum-emitting galaxies (e.g., Venemans et al. 2016; Champagne et al. 2018), or of LAEs (e.g., Bañados et al. 2013; Mazzucchelli et al. 2017a; Ota et al. 2018) around a sample of $z \gtrsim 6$ quasars. The observed [C II]-bright companion galaxies have been considered as potential progenitors of $z \sim 4$ red-and-dead galaxies (Decarli et al. 2017). Previous optical/NIR observations have failed to detect rest-frame UV/optical emission from any of these companion galaxies, suggesting that they are heavily obscured and limiting the study of their overall physical properties (Decarli et al. 2017).

In this work, we present new sensitive optical/NIR follow-up observations obtained from several ground- and space-based facilities, specifically designed to probe companion galaxies to four $6 < z < 6.6$ quasars. In particular, we aim to observe the bulk of their stellar emission in the rest-frame optical wavelength range (~ 5000–7000 Å), in order to assess their total stellar mass (M_*). We also aim to measure their rest-frame UV radiation (~ 1200–1500 Å), to probe the contribution from the young stellar population, and to determine how much of the star formation is unobscured. We observed the fields around three quasars presented in Decarli et al. (2017): SDSS J0842+1218, PSO J231.6576−20.8335, and CFHQS J2100−1715 (hereafter J0842, PJ231, and J2100, respectively), and around

PSO J167.6415−13.4960 (hereafter PJ167; Venemans et al. 2015b; Willott et al. 2017). In the following sections, we will refer to each of the respective companions as "quasar_short_name"c. We also obtained data for a millimeter-bright source, detected only in the dust continuum emission, close to the quasar VIK J2211−3206 (hereafter J2211; B. Venemans et al. 2019, in preparation).[13] This galaxy is part of the sample of dust-continuum-emitting sources discovered around several $z \sim 6$ quasars by Champagne et al. (2018), for which no redshift confirmation is available. We present our follow-up data and discuss our constraints on the properties of this source in Appendix A.

This paper is structured as follows. In Section 2 we present our observations and data reduction. In Section 3.1 we compare the companion galaxies' photometry with the spectral energy distributions (SEDs) of local galaxies, and in Section 3.2 we estimate the (un)obscured star formation rates from the rest-frame (UV) optical emission. In Section 3.3 we place the M_* and SFR of the companions in the context of observations of SMGs and normal star-forming galaxies at comparable redshifts. Finally, in Section 4 we present our conclusions and outlook.

The magnitudes reported in this work are in the AB system. We use a ΛCDM cosmology with $H_0 = 70$ km s^{-1} Mpc^{-1}, $\Omega_m = 0.3$, and $\Omega_\Lambda = 0.7$.

2. Observations and Data Reduction

We collect available observations of the fields in our sample, either from the literature or obtained with dedicated follow-up campaigns. The coordinates, redshifts, spatial and velocity separations of the quasars, and their companion galaxies are reported in Table 1. Details on the optical/NIR observations used here, i.e., dates, instruments/telescopes, exposure times and filters, are shown in Table 2.

2.1. Optical/NIR Spectroscopy

We collected optical and NIR spectroscopic data for the quasars and their respective companions.

We observed the quasars PJ231 and J2100 with the Multi Unit Spectroscopic Explorer (MUSE; Bacon et al. 2010) at the Very Large Telescope (VLT), imaging a total field of view of 1×1 arcmin^2, with a spatial resolution of $0''\!.2$ pixel^{-1} and a

---

[13] This quasar was also recently independently discovered by Chehade et al. (2018), with the name of VST-ATLAS J332.8017−32.1036.

Name	Date/Program ID	Telescope/Instrument	Filters/λ Range	Exp. Time
SDSS J0842+1218[a]	2016 May 8/10	LBT/MODS	0.51–1.06 μm	1320 s
	2016 Mar 15	Magellan/FIRE	0.82–2.49 μm	4176 s
	2017 Apr 27/14876	*HST*/WFC3	F140W	2612 s
	2011 Jan 22/12184	*HST*/WFC3	F105W	356 s
	2017 Feb 9/13066	*Spitzer*/IRAC	3.6, 4.5 μm	7200 s
	2007 Nov 24/40356	*Spitzer*/IRAC	5.8, 8 μm	1000 s
PSO J167.6415–13.4960	2017 Aug 11/14876	*HST*/WFC3	F140W	2612 s
	2017 Apr 13/13066	*Spitzer*/IRAC	3.6, 4.5 μm	7200 s
PSO J231.6576–20.8335	2017 Jul 2/099.A-0682	VLT/MUSE	0.465–0.93 μm	10,656 s
	2016 Mar 15	Magellan/FIRE	0.82–2.49 μm	4788 s
	2017 Apr 1/14876	*HST*/WFC3	F140W	2612 s
	2016 Nov 25/13066	*Spitzer*/IRAC	3.6, 4.5 μm	7200 s
CFHQS J2100–1715	2016 Aug 25/26/297.A-5054	VLT/MUSE	0.465–0.93 μm	7956 s
	2016 Sep 18/19/334041	LBT/LUCI	*J*	10,440 s
	2017 May 4/14876	*HST*/WFC3	F140W	2612 s
	2017 Jan 14/13066	*Spitzer*/IRAC	3.6, 4.5 μm	7200 s
VIK J2211–3206	2017 Apr 28/14876	*HST*/WFC3	F140W	2612 s
	2017 Jan 29/13066	*Spitzer*/IRAC	3.6, 4.5 μm	7200 s

Note. Observations of the dust-continuum detected source close to the quasar VIK J2211–3206 are described in Appendix A.
[a] Archival *Spitzer*/IRAC [5.8], [8.0] and *HST*/WFC3 F105W data are taken from Leipski et al. (2014).

spectral coverage between 4650 Å and 9300 Å. We observed the field of the quasar J2100 using Director's discretionary time (Program ID: 297.A-5054(A), PI: Decarli) during the nights of 2016 August 25 and 26. Sky conditions were good, with seeing varying from 0″8 to 1″3. PJ231 was observed on 2017 July 2 as a part of our program 099.A-0682A (PI: Farina) in almost photometric sky conditions and median seeing of 0″8. We reduced the data using the MUSE Data Reduction Software (Weilbacher et al. 2012, 2014). The final cubes were then post-processed as in Farina et al. (2017). In particular, the pipeline-produced variance cube was rescaled to match the observed variance of the background at each wavelength channel. This allowed us to compute more realistic errors that reflect possible correlations between neighboring voxels. The spectrum of J2100c was extracted with a fixed aperture of 1″ radius centered at the position derived from our ALMA data. In PJ231, the quasar and companion are separated by only 1″5, requiring careful removal of the quasar contribution. We created a point-spread function (PSF) model directly from the quasar by collapsing the spectral region >2000 km s⁻¹ redward of the Lyα line, at a wavelength not contaminated by strong sky emission. At each wavelength channel, the PSF model was rescaled to match the flux of the quasar within 2 spaxels (0″4) of the central emission and then subtracted. The spectrum of the companion was then extracted from this PSF-subtracted data cube with an aperture of 1″ radius. A more detailed analysis of this full data set will be presented in E. P. Farina et al. (in preparation).

We also acquired spectra of the quasar J0842 with the Multi-Object Double Spectrograph (MODS; Pogge et al. 2010) at the Large Binocular Telescope (LBT), in binocular mode on 2016 May 8 and 10. The orientation of the slit covered both the quasar and the [C II] companion galaxy. We used the 1″2 slit and the GG495 filter. We collected two exposures of 1320 s, for a total of 1ʰ28ᵐ on target. Data reduction was performed with standard Python and IRAF procedures. In particular, we corrected for bias

and flat with the modsCCDRed package[14] and we wavelength- and flux-calibrated the data using IRAF. The wavelength scale was calibrated using bright sky emission lines, delivering an accuracy of ∼0.2 Å at λ > 7000 Å. The standard star GD153 was observed to flux-calibrate the data. We further scale the spectrum of the quasar J0842 to match the observed z_{P1} magnitude, as taken from the internal final release, PV3, of the Pan-STARRS1 Survey (z_{P1} = 19.92 ± 0.03, Magnier et al. 2016; see also Jiang et al. 2015 for further details on the discovery and the photometry of this quasar). We applied this scaling to the spectrum of the companion, as extracted with a boxcar filter at the position obtained from the ALMA data.

We observed the companions of PJ231 and J0842, and the quasar PJ231, with the Folded-port InfraRed Echelette (FIRE; Simcoe et al. 2008) at the Magellan Baade Telescope. We observed PJ231 and its companion simultaneously, while we performed a blind offset from the quasar to J0842c. The data were reduced following standard techniques, including bias subtraction, flat field, and sky subtraction. The wavelength calibration was obtained using sky emission lines as reference (see also Bañados et al. 2014). We used the standard stars HIP43018 and HIP70419 to flux calibrate and correct for telluric contamination in the spectra of J0842c and PJ231c, respectively; we implemented the absolute flux calibration considering the *J* magnitude of PJ231 (*J* AB = 19.66 ± 0.05; Mazzucchelli et al. 2017b).

We show all the spectra extracted at the companion positions in Figure 1. No clear emission from any of the companion's spectra is detected. In all cases, we estimated the 3σ limits on the Lyα emission line as:

$$F_{\mathrm{Ly}\alpha,3\sigma} = 3 \times \sqrt{\sum_{i=1}^{N} \mathrm{err}_i^2} \times \sum_{i=1}^{N} \Delta\lambda_i, \qquad (1)$$

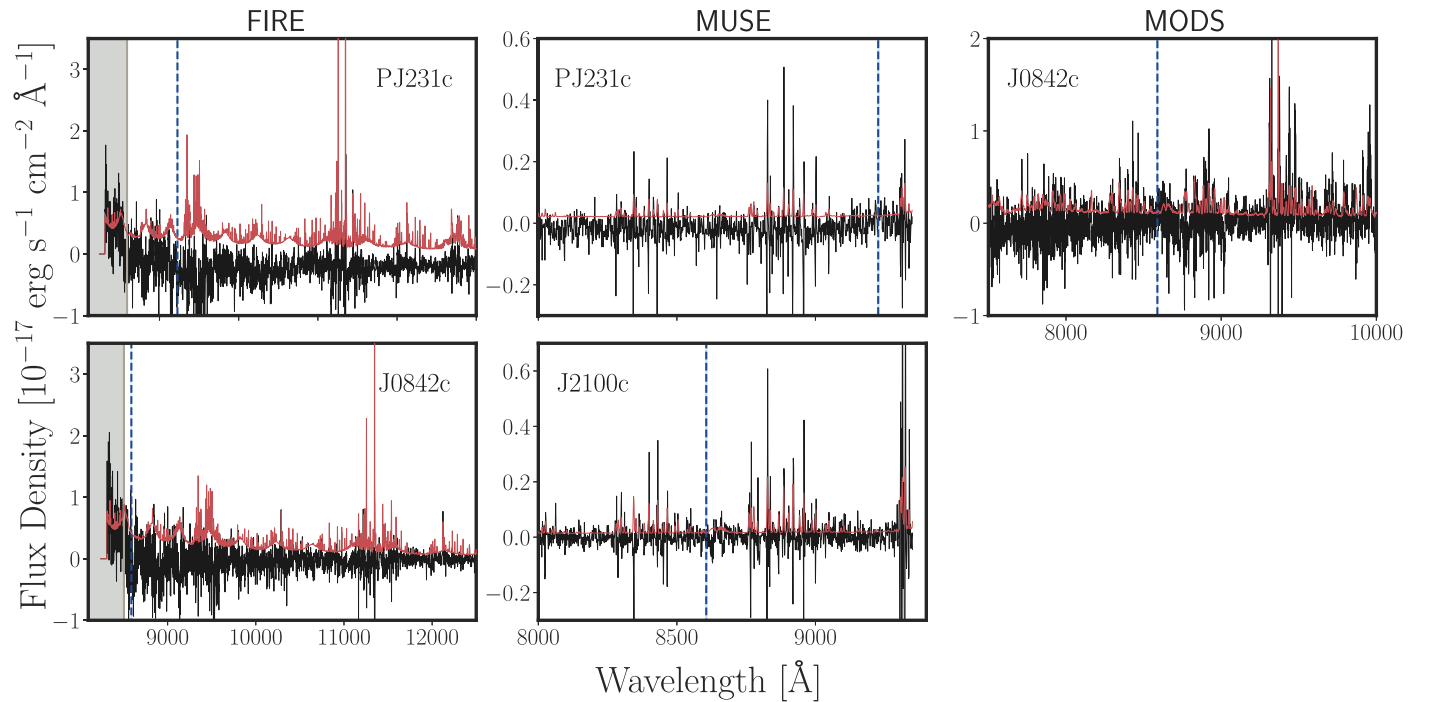[14] http://www.astronomy.ohio-state.edu/MODS/Software/modsCCDRed/

Figure 1. Spectra at the locations of the companions to PJ231, J2100, and J0842, acquired with the FIRE and MODS spectrographs, and extracted from the MUSE data cubes. We highlight the spectral regions where the flux calibration is less reliable with gray shaded areas. Dashed blue lines highlight the expected positions of the respective Lyα emission lines, established from the observations of the narrow [C II] emission with ALMA. The surrounding regions of ±100 km s^{-1} (rest frame), used to estimate limits on the Lyα emission line in the companion galaxies, are also shown with light blue shaded areas.

Table 3
Measurements of the Strength of Lyα Emission Line and of the Underlying Rest-frame UV Continuum from the Spectroscopic Observations of the Companion Galaxies to J0842, PJ231, and J2100, Obtained with VLT/MUSE, Magellan/FIRE, and LBT/MODS

Name	VLT/MUSE		LBT/MODS		Magellan/FIRE	
	$F_{\mathrm{Ly}\alpha}$ (erg s^{-1} cm^{-2})	F_{cont} (erg s^{-1} cm^{-2} Å^{-1})	$F_{\mathrm{Ly}\alpha}$ (erg s^{-1} cm^{-2})	F_{cont} (erg s^{-1} cm^{-2} Å^{-1})	$F_{\mathrm{Ly}\alpha}$ (erg s^{-1} cm^{-2})	F_{cont} (erg s^{-1} cm^{-2} Å^{-1})
SDSS J0842+1218	...		<4.5e−17	<3.0e−16	<2.7e−16	<8.5e−16
PSO J231.6576−20.8335	<2.1e−16	<1.4e−15	...		<1.8e−16	<8.5e−16
CFHQS J2100−1715	<8.3e−17	<3.5e−15	...		...	

Note. Limits are at 3σ significance and obtained as described in Section 2.1.

where err is the error vector, and N is the number of pixels in within a velocity window of (rest frame) 200 km s^{-1} (i.e., the typical line width measured in LAEs, e.g., Ouchi et al. 2008) around the supposed location of the Lyα emission line (as obtained from the ALMA [C II] observations). Finally, $\Delta\lambda = \lambda_{i+1} - \lambda_i$ in the considered wavelength interval. Moreover, we calculated the limits on the underlying continuum emission as:

$$F_{\mathrm{cont},3\sigma} = 3 \times \sqrt{\sum_{i=1}^{N}\mathrm{err}_i^2}, \qquad (2)$$

where we consider here the spectral coverage at hands, excluding noisy regions at the edges. All the estimated values are reported in Table 3.

We note that the emission from the Lyα line in $z \sim 6$–7 LAEs can be redshifted by $\sim$100–200 km s^{-1} with respect to the [C II] line, and/or it can originate from slightly different spatial locations (e.g., Pentericci et al. 2016). Here, the limits we measure by

shifting the center of the Lyα emission by ±150 km s^{-1} are consistent with the fiducial values reported in Table 3, i.e., we do not significantly detect a blue/redshifted line.

2.2. IR Photometry

We list here the observations and data reduction of the imaging follow-up data, obtained with ground- and space-based instruments.

2.2.1. LUCI/LBT

We imaged the field of J2100 in the J band ($\lambda_c = 1.247$ μm and $\Delta\lambda = 0.305$ μm) with the Utility Camera in the Infrared (LUCI1 and LUCI2; Seifert et al. 2003) at the LBT, in binocular mode. We reduced the data following standard techniques, i.e., we subtracted the master dark, divided by the master flat field, and median-combined the frames after subtracting the contribution from the background and after aligning them using field stars. The final astrometric solution
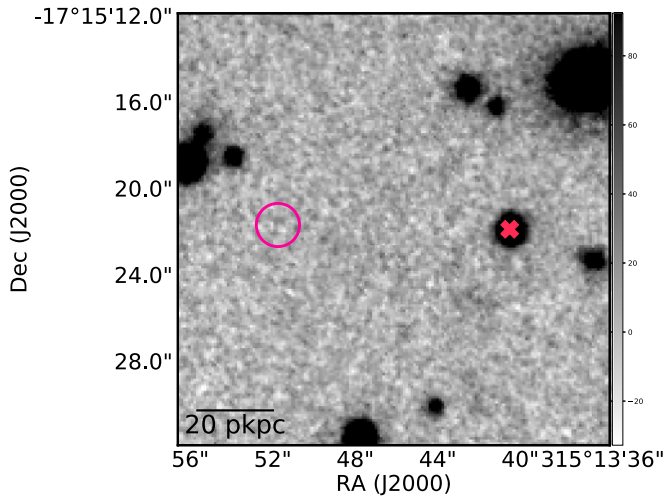
Figure 2. Postage stamp ($20'' \times 20''$) of the field around the quasar J2100, imaged in the J filter with the LUCI1 and LUCI2 cameras at the LBT (see Section 2.2.1 and Table 2). We place a limit of $J > 26.24$ (at 3σ) on the emission from the companion galaxy (magenta circle).

used the *Gaia* Data Release 1 catalog[15] (DR1; Gaia Collaboration et al. 2016a, 2016b) as reference. We flux-calibrated the image with respect to the 2MASS Point Source Catalog. The seeing of the reduced image is $0\rlap{.}''98$. We calculated the depth of the image by distributing circular regions with radius equal to half of the seeing over the frame, in areas with no sources. The 1σ error of our image is the standard deviation of the Gaussian distribution of the fluxes calculated in these apertures. We do not detect, at signal-to-noise ratio (S/N) > 3, any emission at the location of the companion, after performing forced photometry in a circular aperture whose diameter is corresponding to the seeing (see Figure 2). The 3σ limit magnitude that we will use in the following analysis is $J = 26.24$ ($F_J = 0.116\,\mu\text{Jy}$; see Table 4).

2.2.2. WFC3/HST

We obtained new observations of all the targets studied here with the Wide Field Camera 3 (WFC3), on board the *Hubble Space Telescope* (*HST*), using the F140W filter ($\lambda_c = 1.3923\,\mu\text{m}$ and $\Delta\lambda = 0.384\,\mu\text{m}$; Program ID:14876, PI:E. Bañados). For the quasar J0842, previous WFC3 observations in the F105W filter ($\lambda_c = 1.0552$ nm and $\Delta\lambda = 0.265$ nm) were also retrieved from the Hubble Legacy Archive[16] (Program ID:12184, PI: X. Fan). We refer to Table 2 for further details on this data set. We analyzed both the archival and new observations in a consistent way. We considered the reduced data produced by the *HST* pipeline, and we took the zero-point photometry from the WFC3 Handbook.[17] We recalibrated the astrometry using the *Gaia* DR1 catalog (see also Section 2.2.1). We calculated the depth of the images in an analogous way as in Section 2.2.1, considering here circular areas of $0\rlap{.}''4$ radius (containing the 84% of the flux from a point source[18]). We performed aperture photometry using this aperture radius at the positions of the companions. The companion sources of J0842, J2100, and PJ231 were not detected in the F140W filter, and J0842c was

also not detected in the F105W image. We report all the 3σ limit fluxes in Table 4. We show the observations of all the fields studied in this work in the F140W filter in Figure 3, and the F105W image of J0842 in Figure 4. In the case of PJ167, the companion is located at a projected distance of only $0\rlap{.}''9$, and it is blended with the quasar emission. In order to recover meaningful constraints on the brightness of PJ167c, it is necessary to subtract the quasar contribution by modeling the image PSF. We used the bright star 2MASS J11103221−1330007, in the proximity of PJ167, in order to create an empirical PSF model from the same image. This source is located at a distance of only $30''$ from the quasar, limiting the errors due to the changes in the PSF over the field. Its J and H magnitudes from the 2MASS Point Source Catalog are 15.249 and 15.105, respectively. The corresponding $J - H$ color of 0.144 is therefore close to that of the quasar ($J - H = 0.216$). We shifted, scaled, and subtracted the PSF model from the quasar emission using the software GALFIT (version 3.0.5; Peng et al. 2002, 2010). In Figure 5 we show the native *HST* image, the PSF star model, and the residual frame, in which the bright quasar emission has been subtracted. The companion galaxy is well isolated, and its F140W PSF magnitude, measured with GALFIT, is equal to 25.48 ± 0.17 ($F_{\text{F140W}} = 0.23^{+0.04}_{-0.03}\,\mu\text{Jy}$). Diffuse emission extending from the companion to the quasar is also tentatively recovered. Additional, high-resolution imaging and spectroscopy are needed to securely confirm and characterize such emission.

2.2.3. IRAC/Spitzer

The fields of all the objects in our sample were observed in the [3.6] ($\lambda_c = 3.550\,\mu\text{m}$ and $\Delta\lambda = 0.750\,\mu\text{m}$) and [4.5] ($\lambda_c = 4.493\,\mu\text{m}$ and $\Delta\lambda = 1.015\,\mu\text{m}$) filters with the InfraRed Array Camera (IRAC; Fazio et al. 2004; Program ID:13066, PI: C. Mazzucchelli; see Table 2). We also use archival data of J0842 (Program ID:40356, PI: X. Fan), covering the IRAC filters [5.8] ($\lambda_c = 5.731\,\mu\text{m}$ and $\Delta\lambda = 1.425\,\mu\text{m}$) and [8.0] ($\lambda_c = 7.872\,\mu\text{m}$ and $\Delta\lambda = 2.905\,\mu\text{m}$; see Table 2).

We adopt the reduced data from the *Spitzer* pipeline, and the photometric calibration (i.e., photometric zero-point and aperture correction values) specified in the IRAC Instrument Notebook.[19] As in the case of the *HST*/WFC3 observations, we refine the astrometric solution using the recent *Gaia* DR1 catalog. Given the limited spatial sampling of the IRAC camera ($0\rlap{.}''6\,\text{pixel}^{-1}$) and the depth of our [3.6] and [4.5] images, the companion galaxies studied here are blended either with the much brighter quasar, or with foreground sources (see Figure 3). Hence, one needs to properly model and remove these sources. In order to model the PSF, which is undersampled in the IRAC data, we resample the native images over a grid of $0\rlap{.}''12\,\text{pixel}^{-1}$ resolution, using the IRAF task *magnify*. In each magnified image, we select a collection of stars identified as such in the *HST*/WFC3 data within $1' \times 1'$ of the quasar. We obtain the final PSF model for each image by shifting, aligning, scaling, and combining the images of the selected stars. The number of stars used in each field ranges between 4 and 9. We use GALFIT to sample the PSF image to the original resolution ($0\rlap{.}''6\,\text{pixel}^{-1}$), and to model and subtract the emission from the quasar and any foreground objects. In Figure 3, we show the postage stamps of the IRAC [3.6] and [4.5] images, and the corresponding images of the residuals. No clear emission from

---

[15] https://www.cosmos.esa.int/web/gaia/dr1
[16] https://hla.stsci.edu/
[17] http://www.stsci.edu/hst/wfc3/analysis/ir_phot_zpt
[18] http://www.stsci.edu/hst/wfc3/analysis/ir_ee

[19] http://irsa.ipac.caltech.edu/data/SPITZER/docs/irac/iracinstrumenthandbook/IRAC_Instrument_Handbook.pdf

Table 4
Photometric Measurement of the Companion Galaxies to $z \sim 6$ Quasars Studied in This Work (See Section 2)

Name	F_J (μJy)	F_{F105W} (μJy)	F_{F140W} (μJy)	$F_{3.6\ \mu m}$ (μJy)	$F_{4.5\ \mu m}$ (μJy)	$F_{5.8\ \mu m}$ (μJy)	$F_{8.0\ \mu m}$ (μJy)	$F_{1.2\ mm}$ (mJy)
SDSS J0842+1218c	⋯	<0.154	<0.061	<0.78	<1.06	<9.54	<12.6	0.36 ± 0.12
PSO J167.6415−13.4960c	⋯	⋯	$0.23^{0.04}_{0.03}$	<0.78	<1.28	⋯	⋯	0.16 ± 0.03[a]
PSO J231.6576−20.8335c	⋯	⋯	<0.053	<0.64	<2.79	⋯	⋯	1.73 ± 0.16
CFHQS J2100−1715c	<0.116	⋯	<0.083	<0.53	<1.07	⋯	⋯	2.05 ± 0.27

Note. The limits provided are at 3σ significance.
[a] This flux measurement comes from recent $0\rlap{.}''35$, i.e., $\sim$2 pkpc at $z \sim 6.5$, ALMA observations (Neeleman et al. 2019).

the companion galaxies is detected in any of the residual images. We quantify the limits on the photometry of the companions as follows. For each image, we run GALFIT subtracting a source at the exact position of the companion modeled as a PSF and scaled to a fixed magnitude, which we vary between 21 and 25, in steps of 0.01 mag. When adopting magnitudes smaller (i.e., brighter fluxes) than the limit flux to which our image is sensitive, the subtraction will leave a negative residual. We perform aperture photometry in the residual image at the companion position in an aperture of $2\rlap{.}''4$ radius, and we compare the measured flux with the image 3σ flux limit. The adopted flux limit was measured on the same area used for the forced photometry, and by evaluating the background rms in an annulus of radius $14''$ and width of $10''$ centered on the companion. We assume that the 3σ limit magnitude is the value at which the measured absolute flux in the residual image is equal to the 3σ flux limit. We report these values in Table 4.

Finally, we analyze the archival J0842 *Spitzer*/IRAC observations (see Figure 4), which are much shallower (see Table 2), because they were designed only to detect the bright quasar. No foreground objects overlap the companion location, and we therefore perform aperture photometry on the native images, using the same aperture as in the observations in the [3.6] and [4.5] channels. We do not detect any source at S/N > 3. We report the corresponding flux limits in Table 4.

3. Analysis

In this section, we characterize the SEDs of four companions to $z \sim 6$ quasars, by comparing them with a few examples of local galaxies and by modeling their emission with an SED fitting code. We estimate (or set upper limits to) their unobscured/obscured star formation activity observed in the rest-frame UV/IR range. Finally, we place our measurements in the context of observations of star-forming galaxies and starbursts at similar redshift.

3.1. Spectral Energy Distribution

We first compare the SEDs of our companions with those of prototypical galaxies in the local universe. We consider the SEDs of normal star-forming spiral galaxies (M51 and NGC 6946), starbursts (M82), and ultraluminous infrared galaxies (ULIRGs; Arp 220), from Silva et al. (1998). M51 is a nearby ($D = 9.6$ Mpc) spiral (Sbc) interacting galaxy, which has been studied in detail over a wide range of wavelength and physical scales (e.g., Leroy et al. 2017). NGC 6946, found at a distance of 6.72 Mpc, is an intermediate (Scd) spiral galaxy (Degioia-Eastwood et al. 1984). Its size is approximately a third of that of our Galaxy and it hosts roughly half of the stellar mass (e.g., Engargiola 1991). M82

is a prototypical edge-on starburst (with a galaxy-wide SFR $\sim$ 10–30 $M_\odot$ yr^{-1}; Forster Schreiber et al. 2003), whose intense activity has been most probably triggered by a past interaction with the neighboring galaxy M81 (e.g., Yun et al. 1994). Arp 220 is one of the closest (77 Mpc) and best studied ULIRGs, with a total infrared luminosity of $L_{IR} = 1.91 \times 10^{12} M_\odot$ (Armus et al. 2009). It is thought to be the result of a merger that happened $\sim$3–5 Myr ago (e.g., Joseph & Wright 1985; Baan & Haschick 1995; Scoville et al. 1998; Downes & Eckart 2007), and has extreme conditions in its nucleus (e.g., with an attenuation of $A_V = 2 \times 10^5$ mag; Scoville et al. 2017)

Here, we shift the observed SEDs of these local galaxies to the redshifts of the companions, and we scale them to match the 1.2 mm flux retrieved in the ALMA observations. We plot the SEDs, together with the photometry of the companions presented here, in Figure 6.

The limits on rest-frame UV/optical brightness of PJ231c, J2100c, and J0842c rule out all the galaxy templates considered here, with the exception of Arp 220. These companions have infrared luminosities in the range of (ultra-)luminous galaxies (e.g., $(0.9–5) \times 10^{12} L_\odot$; Decarli et al. 2017). On the other hand, the rest-frame UV emission of PJ167c is detected in our *HST*/WFC3 observations (see Section 2). Its UV-to-submilli-meter ratio is comparable to that of the star-forming galaxy NGC 6946, while the limits from our *Spitzer*/IRAC data suggest that it has lower stellar content.

We compute the star formation rates for PJ231c, J2100c, and J0842c assuming that their SEDs are equivalent to that of Arp 220, shifted in redshift and scaled as in Figure 6. We derive their star formation rates from the dust emission in the rest-frame infrared region (SFR$_{IR}$), assuming that the nonobscured SFR is negligible (see Section 3.2). We calculate the total IR luminosity by integrating the emission from 3 to 1100 μm, and we measure the SFR as SFR $= 1.49 \times 10^{-10} L_{IR}$ (Kennicutt & Evans 2012). The obtained values range between 120 and 700 $M_\odot$ yr^{-1}. We note that, if we had instead assumed a modified blackbody model, $f_\nu \propto B_\nu(T_d \nu^\beta)$, and adopted typical parameters for high-redshift galaxies ($T_d = 47$ K and $\beta = 1.6$; e.g., Beelen et al. 2006; Venemans et al. 2016), we would have derived comparable star formation rate values ($\sim$140–800 $M_\odot$ yr^{-1}; see also Decarli et al. 2017).

We can obtain conservative upper limits on the companion stellar masses by subtracting their gas mass (M_{gas}) from their dynamical mass (M_{dyn}). The latter can be obtained from the widths of the [C II] emission line observed with ALMA (see Decarli et al. 2017). We note, however, that these estimates are based on a number of important assumptions on the companions geometry and dynamics (i.e., they are virialized systems), and that they are obtained from data with a relatively modest resolution of $\sim$1″. We list all dynamical masses in
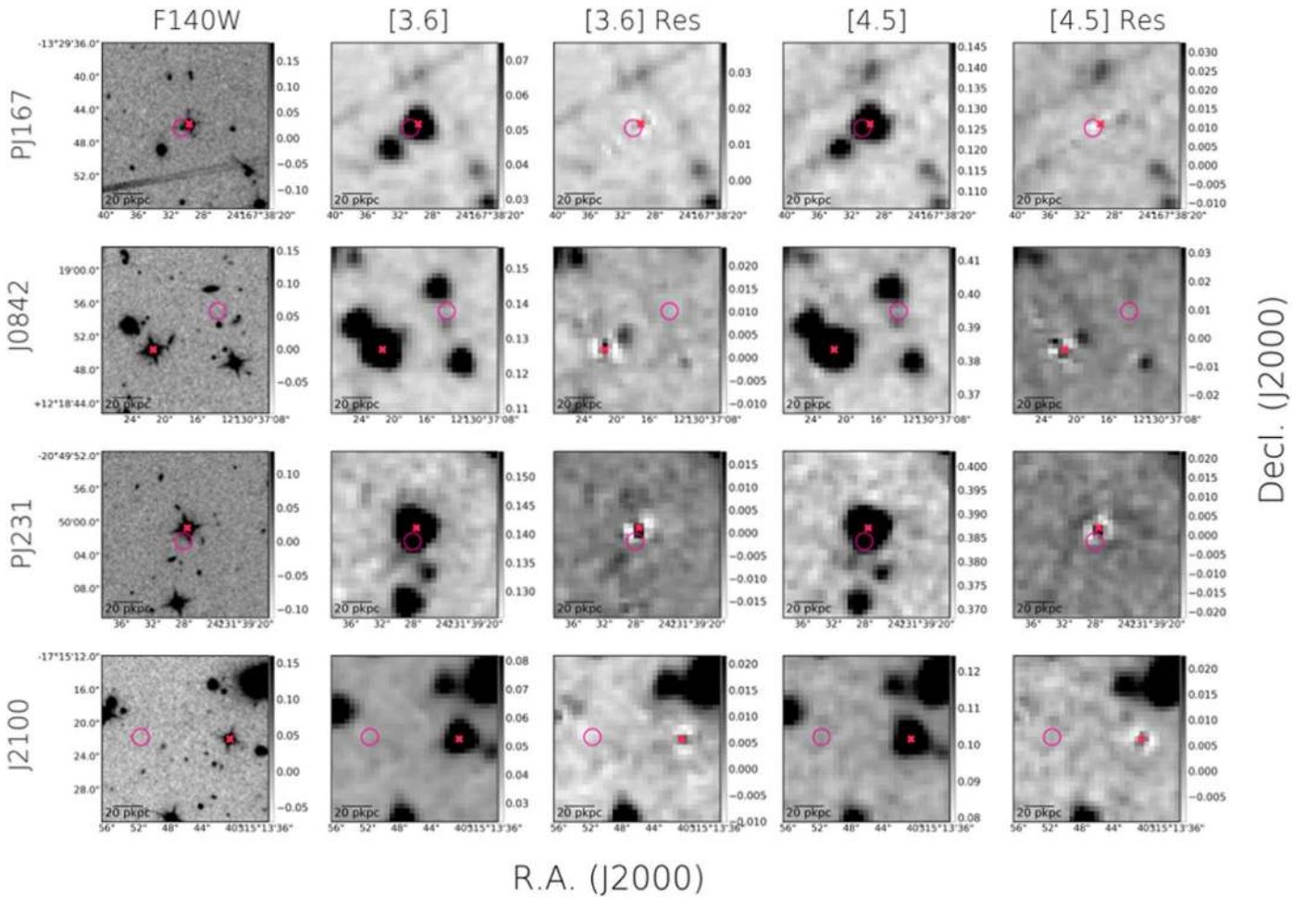
Figure 3. Postage stamps ($20'' \times 20''$) of the four fields (quasar+companion) considered in this study. We also report the residual IRAC images after removing the emission from the quasar and nearby foreground sources (see Section 2.2.3). The positions of the companions and of the quasars are highlighted with magenta circles (of $1''$ radius) and red crosses, respectively.

Table 5. On the other hand, we can estimate M_{gas} from the dust content (M_{dust}). We take these values from Decarli et al. (2017): M_{dust} are measured following the prescription by Downes et al. (1992), while M_{gas} are obtained assuming a typical gas-to-dust ratio of ~ 100 (e.g., Berta et al. 2016). We obtain upper limits on the stellar content ranging between ~ 16 and $21 \times 10^{10} M_{\odot}$. In the following analysis, we utilize the latter values as upper limits on the stellar masses of the companions (see Table 5 and Figures 7 and 8).

Alternatively, we can compare our photometric measurements with synthetic galaxy templates. We use the SED fitting code MAGPHYS (Da Cunha et al. 2008), which uses an energy balance argument to combine simultaneously the radiation from the stellar component, the dust attenuation, and the re-emission in the rest-frame IR wavelength range. We consider here the MAPGPHYS-high-z extension (Da Cunha et al. 2015), which was specifically designed to characterize a sample of SMGs at $3 < z < 6$ (see also Section 3.3). In particular, this version included younger galaxy templates, with higher dust extinction and a wider choice of star formation histories. Nevertheless, fitting the photometry of the companion galaxies presented here with any code is hard, due to the few (and most of the time only one) broadband detections for each source. This is reflected in strong parameter degeneracies in the fit. Another issue is represented by the potentially inappropriate

coverage of the parameter space considered in the fitting machine, which might not be modeling the properties of the peculiar galaxies considered here. Therefore we choose to fit only the companion of PJ167, whose emission is retrieved in more than one broad band. In Figure 6, we show the best-fit template from MAGPHYS-high-z for this galaxy. We take the 50th and 16th/84th percentiles of the marginalized probability distributions as the best-fit values and uncertainties of its SFR and stellar mass. The SED of PJ167c is consistent with that of a star-forming galaxy, SFR $= 53^{+27}_{-19} \, M_{\odot} \, yr^{-1}$, with a stellar mass of $M_* = 0.84^{+0.64}_{-0.40} \times 10^{10} \, M_{\odot}$, a moderate dust extinction ($A_V = 0.66^{+0.35}_{-0.25}$ mag) and a dust content of $M_d = 4.7^{+3.7}_{-1.7} \times 10^7 \, M_{\odot}$.

Finally, we note that, given the close spatial/velocity separation of the companions and the quasar hosts, they are very likely found in physical connection. In particular, PJ167c is located at only $5 \, pkpc/140 \, km \, s^{-1}$ away from PJ167, and emission linking these systems is observed both in the dust continuum and the [C II] line (with a smooth velocity gradient; Decarli et al. 2017; Neeleman et al. 2019) and, tentatively, in the rest-frame UV (see Figure 5). This evidence, together with a measured high velocity dispersion of the cool gas ($\sim 150 \, km \, s^{-1}$; Neeleman et al. 2019) may suggest that these galaxies have already entered an advanced merging stage.
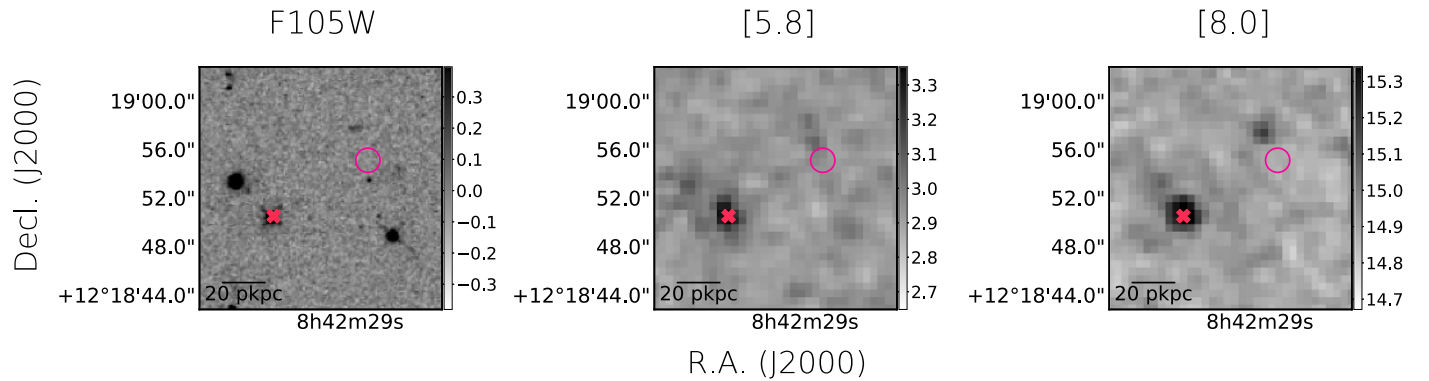
Figure 4. Archival observations ($20'' \times 20''$) of the field around the quasar J0842. The left panel shows the image obtained from the *HST*/WFC3 instrument in the F105W filter, while the other two panels show observations acquired with the *Spitzer*/IRAC camera, in the [5.8] and [8.0] channels (see Section 2.2.3 and Table 2 for references). The quasar is identified with a red cross, while the companion position is highlighted with a magenta circle. These observations were acquired with the aim of studying the bright quasar emission; therefore, the flux limits at the companion position are shallower than the newly obtained images (see Table 4).

3.2. SFR_UV versus SFR_IR

The rest-frame UV emission of galaxies directly traces young stars, i.e., 10–200 Myr old. It is thus an excellent probe of recent star formation, but it is also heavily affected by dust attenuation. The energy of the UV photons is absorbed by the dust, and re-emitted in the IR. Therefore, there also exists a natural correlation between star formation rate and IR emission (see Kennicutt & Evans 2012 for a review).

We here first consider the contribution from the obscured star formation activity, as observed in the rest-frame IR range ($\mathrm{SFR_{IR}}$). For J2100c, J0842c, and PJ231c, we use the values obtained from the Arp 220 SED (see Section 3.1 and Table 5). In the case of PJ167c, we follow the method described in Section 3.1 to derive its $\mathrm{SFR_{IR}}$, but, instead of Arp 220, we use the best SED from the MAGPHYS-high-z fit (see Figure 6 and Table 5). An alternative way of computing the star formation rate is through the luminosity of the [C II] emission line ($L_{\mathrm{[C\,II]}}$; e.g., De Looze et al. 2011, 2014; Sargsyan et al. 2012; Herrera-Camus et al. 2015). Here, we take the values of $\mathrm{SFR_{[C\,II]}}$ reported in Decarli et al. (2017), ranging from ~ 260 to $\sim 730\,M_\odot\,\mathrm{yr}^{-1}$, i.e., of the same order of magnitude as those measured from the dust continuum. For PJ167c, we consider the measurement of the [C II] line from recent high-resolution ALMA observations, i.e., $F_{\mathrm{[C\,II]}} = 1.24 \pm 0.09\,\mathrm{Jy\,km\,s^{-1}}$ (Neeleman et al. 2019). We measured the corresponding [C II] luminosity and star formation rate following Carilli & Walter (2013) and De Looze et al. (2014), respectively. In Table 5 we report all the $\mathrm{SFR_{[C\,II]}}$ values.

On the other hand, we can obtain measurements of (or limits on) the unobscured contribution to the SFR in the companions, using our *HST*/WFC3 sensitive observations in the F140W filter. We consider the conversion between far-UV ($0.155\,\mu\mathrm{m}$) luminosity (L_{FUV}) and $\mathrm{SFR_{UV}}$ provided by Kennicutt & Evans (2012):

$$\log\left[\frac{\mathrm{SFR_{UV}}}{M_\odot\,\mathrm{yr}^{-1}}\right] = \log\left[\frac{L_{\mathrm{FUV}}}{\mathrm{erg\,s^{-1}}}\right] - C_{\mathrm{FUV}} \qquad (3)$$

with $C_{\mathrm{FUV}} = 43.35$. We report in Table 5 the estimated $\mathrm{SFR_{UV}}$ values. The limits achieved by our data are very sensitive, down to a few $M_\odot\,\mathrm{yr}^{-1}$. PJ167c, the only companion detected in the rest-frame UV, has an inferred unobscured star formation rate of $\sim 11\,M_\odot\,\mathrm{yr}^{-1}$. We note that the central wavelength of the broadband filter used here (F140W) corresponds to

$\lambda_{\mathrm{rest}} \sim 0.18$–$0.2\,\mu\mathrm{m}$ for $z \sim 6$–6.6, i.e., in between the classically defined FUV and near-UV (NUV; $0.230\,\mu\mathrm{m}$). In order to check how this impacts our results, we repeat our star formation rate estimates considering the calibration for the NUV ($C_{\mathrm{NUV}} = 43.17$; Kennicutt & Evans 2012). In this case, we measure SFR values only $\sim 1.5\times$ larger. We also consider the best SED fit from MAGPHYS-high-z for PJ167c, and we calculate the star formation rate in the exact FUV range. We obtain $\mathrm{SFR_{UV}} \sim 8\,M_\odot\,\mathrm{yr}^{-1}$, consistent, within the errors, with the one measured directly from our *HST* data.

With the exception of PJ167c, the SFRs measured in the IR in the companions studied here are $\sim$two orders of magnitude larger than the limits we set for the companions rest-frame UV emission. The contribution of $\mathrm{SFR_{UV}}$ to the total star formation budget is therefore negligible. In the case of PJ167c, the unobscured star formation rate is instead only $\sim 6\times$ lower than the obscured one. Another way of performing this comparison is by looking at the fraction of obscured star formation, defined as $f_{\mathrm{obscured}} = \mathrm{SFR_{IR}}/\mathrm{SFR_{IR+UV}}$. Whitaker et al. (2017) reported a tight correlation between this quantity and the stellar mass, irrespective of redshift (up to $z < 2.5$), in a large sample of star-forming galaxies from CANDELS and SDSS. We calculate (limits on) f_{obscured} for the galaxies presented here. We report these values in Table 5, and we show them in the context of previous observations in Figure 7. Again, the star formation rate of the companions is highly dominated by $\mathrm{SFR_{IR}}$, with obscured fractions ranging between 0.74 and 0.99. In particular, taking into account the large uncertainties on M_* and f_{obscured}, PJ167c is consistent with the expectations from lower-redshift studies. The remaining sources seem to also follow the $z < 2.5$ trend (with the caution that we are here only able to set upper limits on their stellar masses).

3.3. SFR versus Stellar Mass

A large number of studies has found a correlation between the SFR and the stellar mass of star-forming galaxies ("main sequence," MS) over a wide redshift range ($0 \lesssim z \lesssim 6$; e.g., Brinchmann et al. 2004; Noeske et al. 2007; Rodighiero et al. 2011; Whitaker et al. 2011; for an in-depth analysis of the literature, see Speagle et al. 2014). The tightness (~ 0.3–0.2 dex scatter) of this relation has been interpreted as evidence that "regular" star-forming galaxies have smooth star formation histories, in which the majority of the mass is assembled via
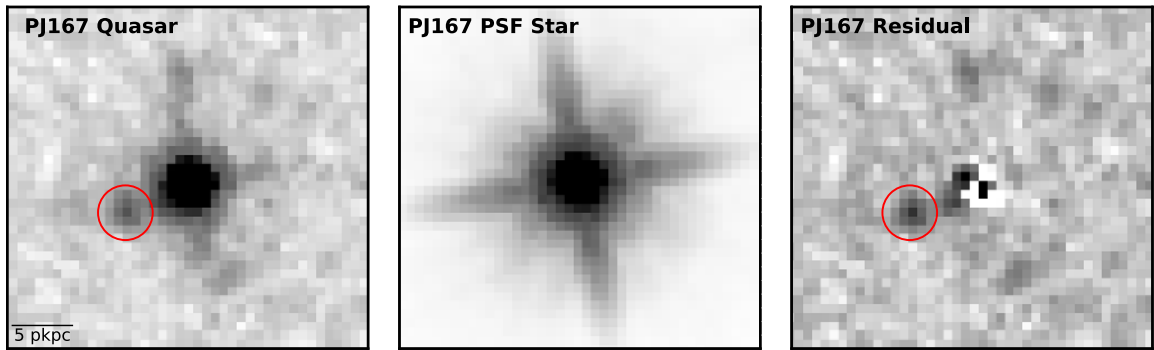
Figure 5. *HST*/WFC3 image in the F140W filter of the quasar PJ167. Left panel: native postage stamp ($5'' \times 5''$). Central panel: empirical PSF model obtained from a bright star in the field (see Section 2.2.2). Right panel: residual image after the subtraction of the empirical PSF from the data. The companion galaxy observed in the ALMA image is detected and well resolved in the latter frame (white circle, of radius $0\rlap{.}''4$). Additional residual flux, located between the center of the bright quasar and the adjacent galaxy is also tentatively detected.
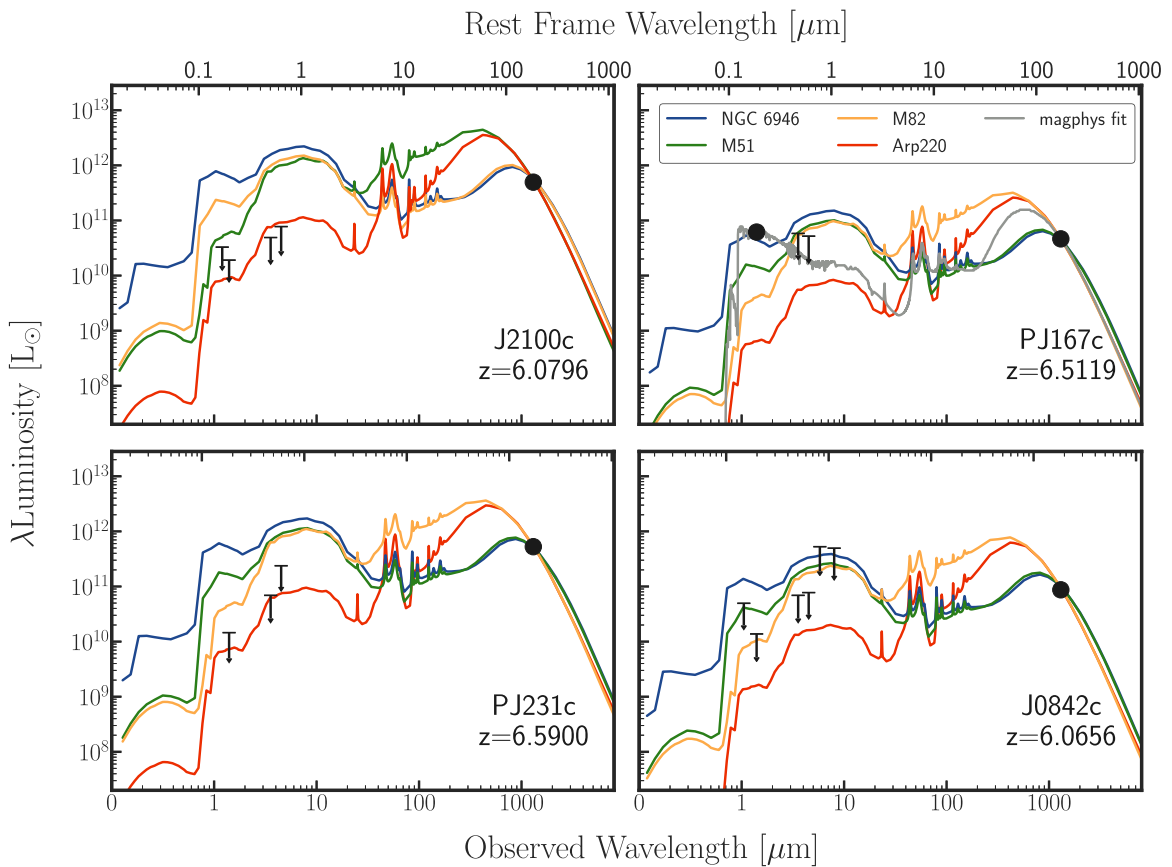
Figure 6. Spectral energy distribution of four companion galaxies adjacent to $z \sim 6$ quasars. The measurements from our photometric observations (Table 4) are reported with down-pointing arrows (limits at 3σ significance) and filled black points. As a comparison, we show representative SEDs of various local star-forming galaxies (NGC 6946, blue; M51, green) and starbursts/ULIRG (M82, orange; Arp 220, red line; Silva et al. 1998), normalized to the ALMA 1.2 mm measurement. The best-fit template (gray line) of the SED of PJ167c, obtained with the code MAPGPHYS-high-z (Da Cunha et al. 2015), is also reported. The SEDs of J2100c, J0842c, and PJ231c are consistent with being Arp 220-like galaxies, i.e., intensely forming stars and highly dust obscured, at $z \sim 6$. The *HST*/WFC3 measurement of the rest-frame UV emission of PJ167c suggests that this source is more similar to a "regular" star-forming galaxy (e.g., NGC 6964), with a lower stellar mass.

steady accretion of cool gas from the intergalactic medium on long timescales (e.g., Daddi et al. 2007; Steinhardt et al. 2014). On the other hand, highly starbursting galaxies, which lie above the MS, are also observed, and are thought to grow mainly via efficient, merger-triggered star formation events (e.g., Santini et al. 2014). The MS normalization is observed to evolve with redshift, and this trend suggests that higher specific star formation rates are common at early cosmic times (e.g., Whitaker et al. 2014).

We compare the properties of the companion galaxies considered here with those of typical star-forming galaxies and SMGs at similar redshifts (see Figure 8). We consider the observed MS relation at $z \sim 6$ provided by Salmon et al. (2015) and Speagle et al. (2014), together with predictions from semianalytical models by Somerville et al. (2008, 2012). Salmon et al. (2015) examine $3.5 \leqslant z \leqslant 6.5$ galaxies in the GOODS-S field: we take here SFR and M_* values of their

Table 5
Physical Properties of the Companion Galaxies to $z \sim 6$ Quasars Studied in This Work

Name	SFR$_{UV}$ ($M_\odot$ yr^{-1})	SFR$_{IR}$ ($M_\odot$ yr^{-1})	SFR$_{[C\,II]}$ ($M_\odot$ yr^{-1})	$f_{obscured}$ = SFR$_{IR}$/SFR$_{UV+IR}$	M_{dyn} ($\times 10^{10}\,M_\odot$)	M_* ($\times 10^{10}\,M_\odot$)
SDSS J0842+1218c	<2	124 ± 54	260 ± 40	>0.98	12 ± 5	<11
PSO J167.6415−13.4960c	11 ± 3	32 ± 4	182 ± 16	0.74 ± 0.20	⋯	$0.84^{+0.64}_{-0.40}$
PSO J231.6576−20.8335c	<3	709 ± 157	730 ± 100	>0.99	22 ± 8	<16.8
CFHQS J2100−1715c	<3	573 ± 73	360 ± 70	>0.99	27 ± 13	<21.5

Note. We report the unobscured (rest-frame UV) SFRs calculated from our *HST*/WFC3 observations (Section 3.2), and the obscured (rest-frame IR) contribution from our ALMA data (Sections 3.1 and 3.2). Finally, the dynamical mass estimates and upper limits on the stellar masses are also listed. In the case of PJ167c, the reported stellar mass is that derived from MAGPHYS-high-z (see Section 3.1). We note that the SFR$_{[C\,II]}$ values have an additional uncertainty of 0.5 dex due to the scatter around the relationship from De Looze et al. (2014).
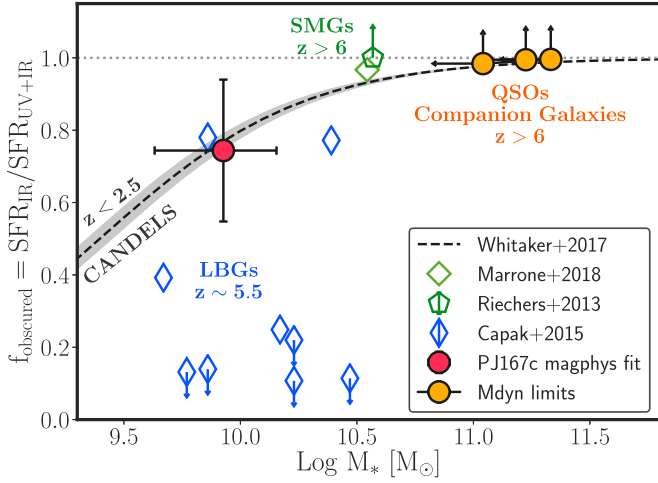
Figure 7. Fraction of obscured star formation as a function of stellar mass. A tight correlation is observed at lower redshifts ($0 < z < 2.5$; dashed black line, Whitaker et al. 2017). We show the location of $z > 6$ SMGs observed by Marrone et al. (2018; big diamond) and Riechers et al. (2013; pentagon), together with $z \sim 5.5$ LBGs from Capak et al. (2015; blue diamond). The galaxies studied in this work are reported with red (PJ167c, whose physical properties were obtained with the code MAGPHYS-high-z) and yellow circles (J2100c, PJ231c, J0842c; see Section 3.1). In the latter case, only limits for the unobscured SFR could be derived (see Section 3.2). The star formation of companions to high-z quasars is dominated by the obscured component.

~ 200 $z \sim 6$ galaxies. Speagle et al. (2014) assemble a comprehensive compilation of 25 studies of the MS at $0 \lesssim z \lesssim 6$. After a careful recalibration of the various data sets, they obtain a robust SFR–M_* relation as a function of the age of the universe (t, here in Gyr):

$$\log \text{SFR}[M_*, t] = (0.84 - 0.026 \times t) \log M_* \\ - (6.51 - 0.11 \times t). \quad (4)$$

They also find a scatter around the MS of ~ 0.2 dex, irrespective of redshift. We show this relation, calculated at $z = 6$ with the representative 0.2 dex scatter, in Figure 8. We consider the semianalytical model by Somerville et al. (2012), who use N-body simulations and several feedback/accretion recipes to specifically reproduce the GOODS-S field. In particular, we consider the MS relation for this model at $z \sim 6$, as provided by Salmon et al. (2015; see their Table 4). In addition, we report observed SMGs at $4.5 < z < 6.1$ from Da Cunha et al. (2015), whose redshifts and physical parameters were obtained with MAGPHYS-high-z, and at $z \sim 4.5$ from Gomez-Guijarro et al. (2018), for which recent
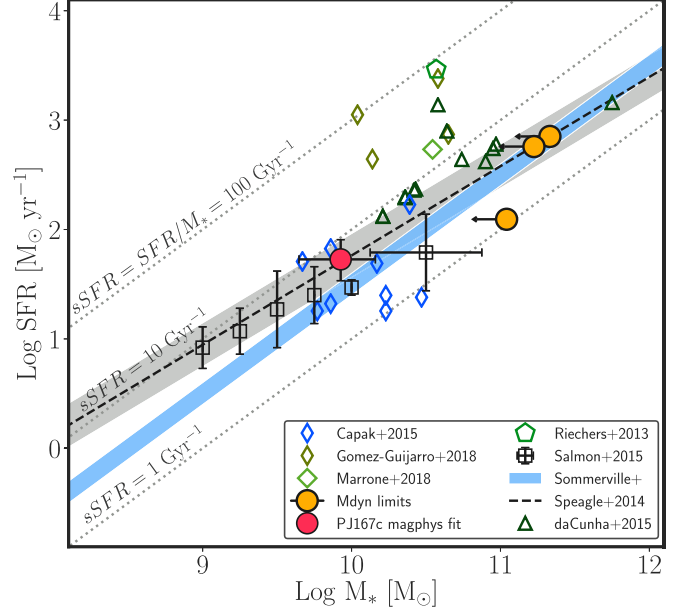

Figure 8. Star formation rate as a function of stellar mass for a compilation of sources at $z \sim 6$. We report observations of the galaxy main sequence (MS) from Salmon et al. (2015; empty black squares), the empirically derived MS relation by Speagle et al. (2014; dashed line and gray region), and the MS location predicted by semianalytical models (Somerville et al. 2012; light blue region). The Speagle et al. relation is based on observations with $M_* < 10^{10.5}\,M_\odot$, and extrapolated linearly at higher masses. We show further examples of submillimeter galaxies, from $z \sim 4.5$–6.1 sources (Da Cunha et al. 2015, triangles, and Gomez-Guijarro et al. 2018, small diamonds) to the extreme starbursts observed at $z = 6.3$ (Riechers et al. 2013; pentagon) and at $z = 6.9$ (Marrone et al. 2018; big diamond), and $z \sim 5.5$ LBGs from Capak et al. (2015, blue diamonds). We note that the SFR of the galaxies taken from the literature are derived with different methods (see Section 3.3). The companion galaxies reported in this work are shown with red and yellow circles (labels analogous to Figure 7). Finally, we show the loci of constant sSFRs (gray dotted lines). The companion galaxies are consistent with lying on the MS at $z \sim 6$. Deeper observations, particularly in the rest-frame optical region, are necessary to securely characterize the properties of these sources.

ALMA millimeter observations and secure spectroscopic redshifts are available. Finally, we show the massive, extremely starbursting galaxies at $z > 6$ discovered by Riechers et al. (2013) and Marrone et al. (2018; see Section 1), and $z \sim 5.5$ LBGs (Capak et al. 2015).

We show in Figure 8 the SFR and M_* values obtained with MAGPHYS-high-z for PJ167c. This galaxy lies on the MS at $z \sim 6$. For the remaining galaxies, i.e., J2100c, J0842c, and PJ231c, we only consider the obscured star formation rates and the upper limits on the stellar masses (see Section 3.1). These

highly conservative constraints place the companions on or above the MS relation.

Future, deeper observations in the IR regime, together with further development of current fitting machines ,will be needed to constrain these galaxies' SEDs and stellar masses.

4. Conclusions

In this work, we present sensitive follow-up optical and NIR imaging and spectroscopy of companion galaxies adjacent (i.e., <60 kpc and <450 km s^{-1}) to four $z \sim 6$ quasars, initially discovered by their bright [C II] and far-infrared emission with ALMA (Decarli et al. 2017; Willott et al. 2017).

The data reported here have been acquired with several ground- and space-based facilities (i.e., VLT/MUSE, MODS, and LUCI at the LBT, Magellan/FIRE, *Spitzer*/IRAC, and *HST*/WFC3), and are aimed at probing the galaxies' stellar content, recovered in the rest-frame UV/optical regime. We perform aperture photometry at the location of the galaxies (as measured by ALMA), after accounting for both the bright, point-like, nonthermal quasar radiation and any foreground objects. We detect no rest-frame 5000–7000 Å stellar emission (at $>3\sigma$ significance level) from the companions, observed at 3–5 μm. In addition, no light from young stars, probed at $\lambda_{\rm obs} \sim 1.4\ \mu$m by *HST*/WFC3, is detected in three of the four sources examined, i.e., J2100c, J0842c, and PJ231c. However, the companion galaxy of the quasar PJ167 is detected in our *HST* observations at 6.4σ.

From a comparison with SEDs of various local galaxies, we find that the companions PJ231c, J2100c, and J0842c are consistent with an Arp 220-like galaxy at $z \sim 6$. These objects are heavily dust-obscured and/or they harbor a modest stellar mass. The source PJ167c resembles, instead, a less extreme star-forming galaxy. We compute SFRs and M_* with the SED fitting code MAGPHYS-high-z for this galaxy, whose emission is detected in more than one broad band. We derive the obscured SFR of PJ231c, J0842c, and J2100c by assuming the SED of Arp 220 scaled at the observed fluxes. We place upper limits on their stellar masses by subtracting their gas masses, estimated from the dust content, from their total dynamical masses, derived from the [C II] emission line widths. We also derive tight constraints on their unobscured star formation rate, as obtained from the sensitive *HST*/WFC3 data. We observe SFR$_{\rm FUV} \lesssim 3\ M_\odot$ yr^{-1}, i.e., more than two orders of magnitude lower than SFR$_{\rm IR}$, with the exception of PJ167c, whose obscured star formation component is only $\sim 6\times$ larger than the unobscured value. Finally, we find that the companions examined here are consistent with being on the main sequence of star-forming galaxies at $z \sim 6$. However, our constraints/limits, in particular on the stellar masses, are still coarse. This is mainly due to the lack of detections in the bluer bands.

In the near future, deep observations with upcoming instruments, e.g., the NIRCAM and NIRSPEC cameras on board the *James Webb Space Telescope*, will enable us to uncover the emission and dynamics of the stellar content of these galaxies, and, together with updated fitting techniques, to place strong constraints on their SEDs.

Appendix A
Dust-continuum Emitting Source Adjacent to the Quasar VIK J2211–3206

We detect emission from the dust continuum, but not from the [C II] emission line, from a source in the field of the quasar

J2211 (QSO R.A. 22:11:12.39; decl. -32:06:12.9), at redshift $z_{\mathrm{quasar}} = 6.3394 \pm 0.001$ (Decarli et al. 2018). No secure redshift value is measured for this neighboring source (hereafter J2211c). Note that the detection of an object with flux density comparable to J2211c over the area covered in the ALMA survey (Decarli et al. 2018) is expected from a comparison with the number counts of 1.2 mm bright sources observed in blank fields (e.g., Aravena et al. 2016). Indeed, if one integrates the luminosity function of 1.2 mm detected-sources provided by Fujimoto et al. (2016) down to the flux of J2211c (see Table 6), one expects $\sim$2.4 sources in 1 arcmin^2. This amounts to $\sim$9.8 sources in the effective area spanned by our ALMA Survey (i.e., $\sim$4 arcmin^2). This number is consistent with that of sources with similar brightness as J2211c (10) found in the sample recently compiled by Champagne et al. (2018).

We acquired new observations of this field as part of our follow-up campaign of [C II]-bright companions to high-redshift quasars, using *HST*/WFC3 and *Spitzer*/IRAC (see Table 2 for details of the observations). We reduced and analyzed the data following the procedures reported in Section 2. In what follows, we assume that J2211c is located at the redshift of the quasar. No emission from the stellar population in the rest-frame optical regime is measured (at 3σ significance) in the *Spitzer*/IRAC images. However, we tentatively measure (S/N = 2.1) emission in the F140W filter with the *HST*/WFC3 camera. We report our photometric measurements/3σ limits in Table 6, where we also list the galactic properties (coordinates and millimeter flux) obtained from ALMA data (Decarli et al. 2017; Champagne et al. 2018). In Figure 9 we show the postage stamps of our follow-up observations.

In analogy with the companions discussed in the main body of the paper, we compare the SED of J2211c with those of local galaxies, and we fit our photometric data with MAGPHYS-high-z (see Figure 9). From the latter, we find that the SED of J2211c is better reproduced by a galaxy model in between Arp 220 and

Table 6
Information on VIK J2211–3206c, a Source Adjacent to the Quasar J2211 Detected Only via Its Dust Continuum Emission

VIK J2211–3206c	
R.A. (J2000)	22:11:12.11
Decl. (J2000)	-32:06:16.19
$\Delta r_{\mathrm{projected}}$ (kpc)	26.8
F140W (mag)	27.39 ± 0.52
$F_{3.6\,\mu\mathrm{m}}$ (μJy)	<3.42
$F_{4.5\,\mu\mathrm{m}}$ (μJy)	<1.80
F_{mm} (mJy)	0.64 ± 0.06
SFR$_{\mathrm{IR}}$ ($M_\odot$ yr^{-1})	257 ± 36
SFR$_{\mathrm{UV}}$ ($M_\odot$ yr^{-1})	2 ± 2
f_{obscured}	0.99 ± 0.14
SFR$_{\mathrm{magphys}}$ ($M_\odot$ yr^{-1})	132^{+120}_{-59}
$M_{*,\mathrm{magphys}}$ ($M_\odot$)	$2.75^{+3.13}_{-1.47} \times 10^{10}$

Note. Given the lack of any redshift measurement, we are not able to securely identify this galaxy as physically interacting with the quasar, and place it in the context of the analysis of the companions. We report here its coordinates and projected spatial separation to the quasar, obtained from ALMA data (Champagne et al. 2018; Decarli et al. 2018), and our *HST*/WFC3 and *Spitzer*/IRAC follow-up photometric measurements/limits (see Figure 9). We also list our constraints on its physical properties, given the assumption that J2211c lies at the quasar redshift.

M82 (i.e., a powerful local ULIRG and a starburst), with $M_* \sim 3 \times 10^{10}\,M_\odot$ and SFR $\sim 130\,M_\odot$ yr^{-1}. We further measure the obscured/unobscured SFR ratio of J2211c, following the procedure used for PJ167c (see Section 3.2). The star formation rate is dominated by the obscured contribution (SFR$_{\mathrm{UV}} \sim 2\,M_\odot$ yr^{-1} and $f_{\mathrm{obscured}} \sim 0.99$). We report all these estimates in Table 6. The lack of a secure redshift confirmation prevents us from drawing further conclusions on the nature of this source, or from placing it in the context of previous observations.
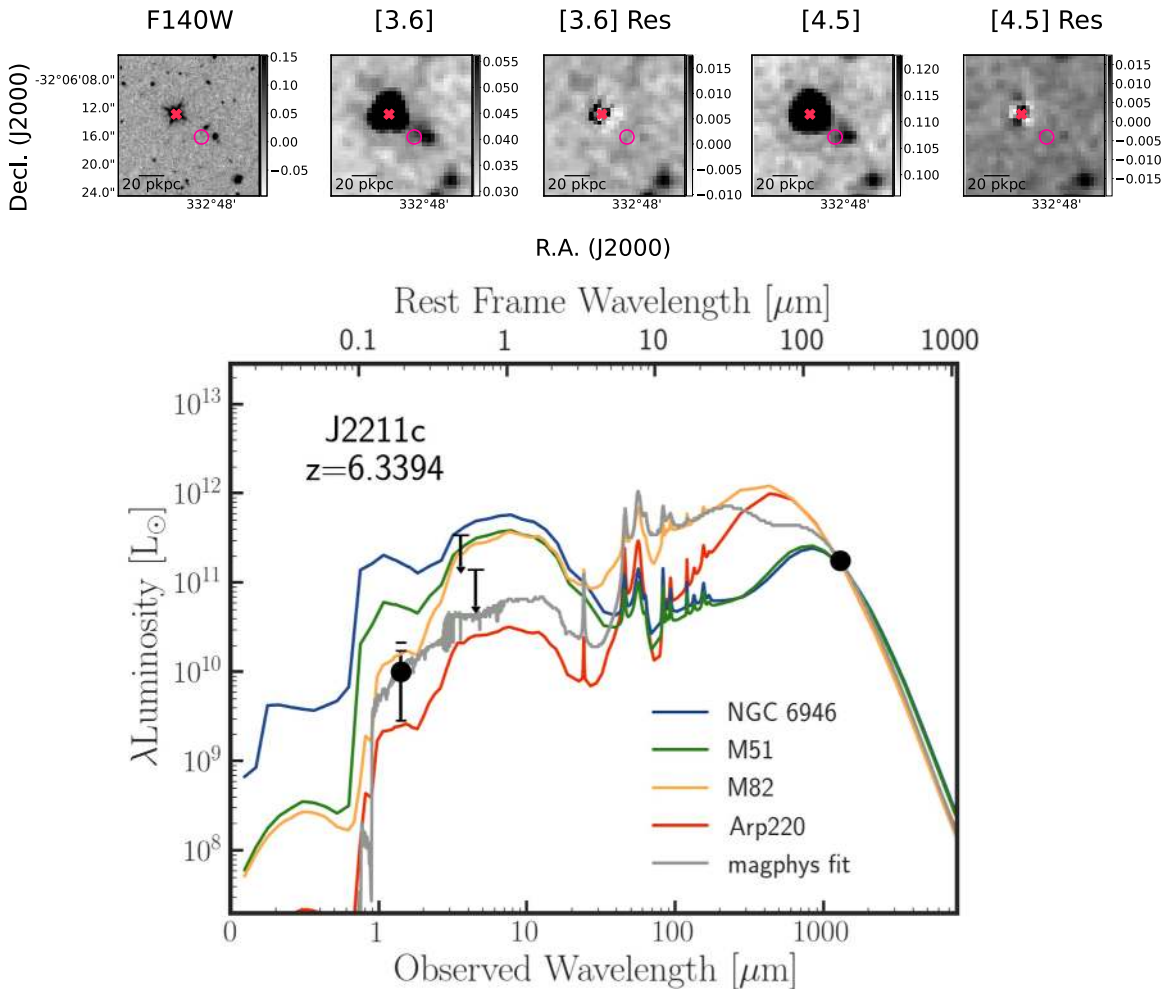
Figure 9. Source adjacent to the quasar J2211, detected solely in the dust-continuum emission, i.e., with no secure redshift measure. Top: postage stamps ($20'' \times 20''$) of our follow-up observations; labels are as in Figure 3. Bottom: spectral energy distribution of J2211c. We assume that the source is located at the same redshift of the quasar. We report our photometric measurements/limits and, for comparison, various templates of local galaxies and the best SED fit from MAGPHYS-high-z. The labels and templates are as in Figure 6. J2211c SED results to be intermediate between the low-z ULIRG Arp220 and the starbursting galaxy M82 (see Section 3.1). On the basis of our follow-up observations, and considering the predicted density of millimeter-sources, we are not able to exclude that this source is a fore/background (see the text for details, and Champagne et al. 2018).

Appendix B
Quasar Photometry

In the framework of our study of companion galaxies, we also perform forced photometry at the position of the quasars in the *Spitzer*/IRAC and *HST*/WFC3 images (see Section 2 for methodology). In Table 7 we report the derived quasars'

photometry. In Figure 10, we show the quasars SEDs. The fluxes measured in our follow-up data are consistent with those expected from the observed optical/NIR spectra, when available, and/or from a lower-z quasar template (Selsing et al. 2016) rescaled to match the observed *J* band magnitude.
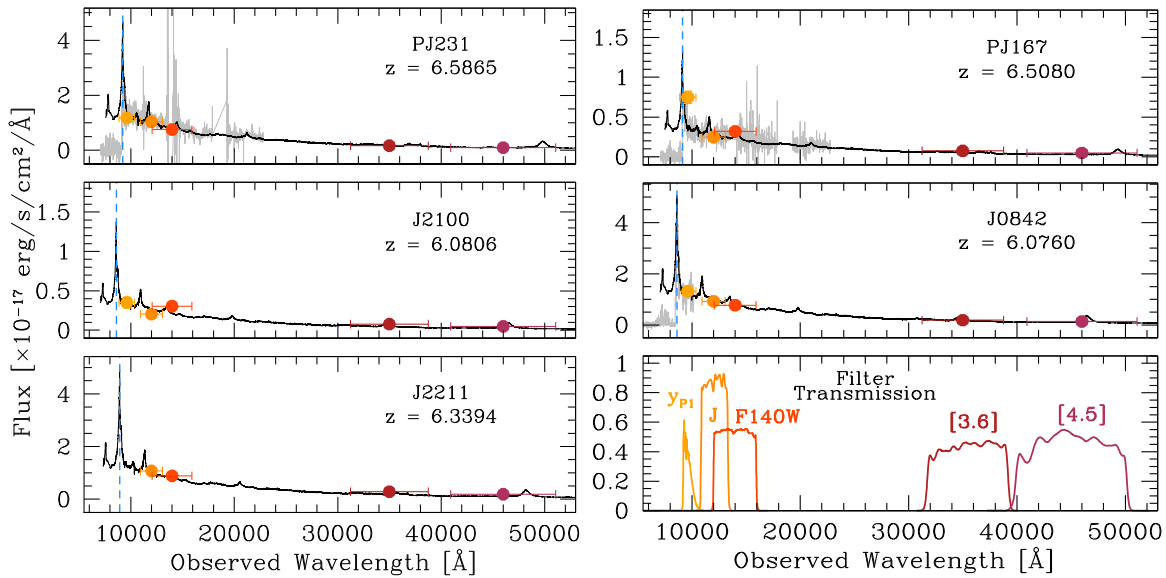
Figure 10. Spectral energy distribution of the quasars in our sample. The observed photometric measurements (filled points) are obtained from our new follow-up data and from the literature (see Table 7; the filter responses are reported in the lower right panel). We also show the available optical/NIR spectra (light gray; see also Mazzucchelli et al. 2017b), and a lower-redshift composite template shifted at the redshift of the quasar (black solid line; Selsing et al. 2016). The location of the Lyα line is highlighted with a light blue dashed line.

Table 7
Photometric Measurements of the Quasars Studied in This Work (see Section 2)

Name	$F_{y_{P1}}$ (mJy)	F_J (mJy)	F_{F140W} (mJy)	$F_{3.6\ \mu m}$ (mJy)	$F_{4.5\ \mu m}$ (mJy)	$F_{1.2\ mm}$ (mJy)	References J
SDSS J0842+1218	$40.55^{+2.3}_{-2.2}$	44.46 ± 1.2	50.19 ± 0.02	76.29 ± 0.22	93.33 ± 0.25	0.87 ± 0.18	(1)
PSO J167.6415–13.4960	$23.12^{+2.5}_{-2.2}$	11.91 ± 1.0	20.89 ± 0.02	30.56 ± 0.23	34.32 ± 0.17	0.87 ± 0.05	(2)
PSO J231.6576–20.8335	$36.31^{+2.8}_{-2.6}$	$49.66^{+2.3}_{-2.2}$	49.13 ± 0.02	66.95 ± 0.22	67.91 ± 0.22	4.41 ± 0.16	(3)
CFHQS J2100–1715	$10.86^{+2.3}_{-1.9}$	9.82 ± 0.9	19.95 ± 0.02	31.65 ± 0.25	34.76 ± 0.26	1.20 ± 0.15	(4)
SDSS J2211–3206	$\cdots$	$51.52^{+5.0}_{-4.5}$	57.93 ± 0.02	116.05 ± 0.23	131.45 ± 0.19	0.57 ± 0.05	(5)

Note. The measurements in the y_{P1} band are from the PS1 PV3 catalog, while the J band values are from (1) Jiang et al. (2015), (2) Venemans et al. (2015b), (3) Mazzucchelli et al. (2017b), (4) Willott et al. (2010), and (5) B. Venemans et al. (2019, in preparation).

ORCID iDs

C. Mazzucchelli https://orcid.org/0000-0002-5941-5214
R. Decarli https://orcid.org/0000-0002-2662-8803
E. P. Farina https://orcid.org/0000-0002-6822-2254
E. Bañados https://orcid.org/0000-0002-2931-7824
B. P. Venemans https://orcid.org/0000-0001-9024-8322
M. A. Strauss https://orcid.org/0000-0002-0106-7755
F. Walter https://orcid.org/0000-0003-4793-7880
M. Neeleman https://orcid.org/0000-0002-9838-8191
F. Bertoldi https://orcid.org/0000-0002-1707-1775
X. Fan https://orcid.org/0000-0003-3310-0131
D. Riechers https://orcid.org/0000-0001-9585-1462
H.-W. Rix https://orcid.org/0000-0003-4996-9069
R. Wang https://orcid.org/0000-0003-4956-5742

References

Angulo, R. E., Springel, V., White, S. D. M., et al. 2012, MNRAS, 425, 2722A
Aravena, M., Decarli, R., Walter, F., et al. 2016, ApJ, 833, 68
Armus, L., Mazzarella, J. M., Evans, A. S., et al. 2009, PASP, 121, 559
Baan, W. A., & Haschick, A. D. 1995, ApJ, 454, 745
Bacon, R., Accardo, M., Adjali, L., et al. 2010, Proc. SPIE, 7735, 773508
Bañados, E., Venemans, B., Morganson, E., et al. 2014, AJ, 148, 14
Bañados, E., Venemans, B., Walter, F., et al. 2013, ApJ, 773, 178
Bañados, E., Venemans, B. P., Decarli, R., et al. 2016, ApJS, 227, 11

Bañados, E., Venemans, B. P., Mazzucchell, C., et al. 2018, Natur, 553, 473
Beelen, A., Cox, P., Benford, D. J., et al. 2006, ApJ, 642, 694
Berta, S., Lutz, D., Genzel, R., et al. 2016, A&A, 587, A73
Blain, A. W., Smail, I., Ivison, R. J., et al. 2002, PhR, 369, 111
Brinchmann, J., Charlot, S., White, S. D. M., et al. 2004, MNRAS, 351, 1151
Capak, P. L., Carilli, C., Jones, G., et al. 2015, Natur, 522, 455
Carilli, C., & Walter, F. 2013, ARA&A, 51, 105C
Champagne, J. B., Decarli, R., Casey, C. M., et al. 2018, ApJ, 867, 153
Chehade, B., Carnall, A. C., Shanks, T., et al. 2018, MNRAS, 478, 1649
Da Cunha, E., Charlot, S., & Elbaz, D. 2008, MNRAS, 388, 1595
Da Cunha, E., Walter, F., Smail, I. R., et al. 2015, ApJ, 806, 110
Daddi, E., Dickinson, M., Morrison, G., et al. 2007, ApJ, 670, 156
De Looze, I., Baes, M., & Bendo, G. J. 2011, MNRAS, 416, 2712
De Looze, I., Cormier, D., & Lebouteiller, V. 2014, A&A, 568, A62
Decarli, R., Walter, F., Venemans, B. P., et al. 2017, Natur, 545, 457
Decarli, R., Walter, F., Venemans, B. P., et al. 2018, ApJ, 854, 97
Decarli, R., Walter, F., Yang, Y., et al. 2012, ApJ, 756, 150
Degioia-Eastwood, K., Grasdalen, G. L., Strom, S. E., & Strom, K. M. 1984, ApJ, 278, 564
Diaz-Santos, T., Armus, L., Charmandaris, V., et al. 2017, ApJ, 846, 32
Downes, D., & Eckart, A. 2007, A&A, 468, L57
Downes, D., Radford, J. E., Greve, A., et al. 1992, ApJ, 398L, 25
Engargiola, G. 1991, ApJS, 76, 875
Fan, X., Strauss, M., & Becker, R. H. 2006, AJ, 132, 117
Farina, E. P., Venemans, B. P., Decarli, R., et al. 2017, ApJ, 848, 78
Fazio, G. G., Hora, J. L., Allen, L. E., et al. 2004, ApJS, 154, 10
Forster Schreiber, N. M., Genzel, R., Lutz, D., & Sternberg, A. 2003, ApJ, 599, 193
Fudamoto, Y., Ivison, R. J., Oteo, I., et al. 2017, MNRAS, 472, 2028

Fujimoto, S., Ouchi, M., Ono, Y., et al. 2016, ApJS, 222, 1
Gaia Collaboration et al. 2016a, A&A, 595A, 1
Gaia Collaboration et al. 2016b, A&A, 595A, 2
Gomez-Guijarro, C., Toft, S., Karim, A., et al. 2018, ApJ, 856, 121
Herrera-Camus, R., Bolatto, A., Wolfire, M., et al. 2015, ApJ, 800, 1
Herrera-Camus, R., Sturm, E., Gracia-Carpio, J., et al. 2018a, ApJ, 861, 94
Herrera-Camus, R., Sturm, E., Gracia-Carpio, J., et al. 2018b, ApJ, 861, 95
Hodge, J. A., Carilli, C., Walter, F., et al. 2013a, ApJ, 776, 22
Hodge, J. A., Karim, A., Smail, I., et al. 2013b, ApJ, 768, 91
Hopkins, P. F., Hernquist, L., Cox, M., & Keres, D. 2008, ApJS, 175, 356
Jiang, L., McGreer, I., Fan, X., et al. 2015, AJ, 149, 188
Joseph, R. D., & Wright, G. S. 1985, MNRAS, 214, 87
Kennicutt, R. C., & Evans, N. 2012, ARA&A, 50, 531
Leipski, C., Meisenheimer, K., Walter, F., et al. 2014, ApJ, 785, 154
Leroy, A. K., Schinnerer, E., Hughes, A., et al. 2017, ApJ, 846, 71
Magnier, E. A., Schlafly, E. F., Finkbeiner, D. P., et al. 2016, arXiv:1612.05242
Maiolino, R., Caselli, P., Nagao, T., et al. 2009, A&A, 500, L1
Marrone, D. P., Spilker, J. S., Hayward, C. C., et al. 2018, Natur, 553, 51
Matsuoka, Y., Strauss, M. A., Kashikawa, N., et al. 2018, ApJ, 869, 150
Mazzucchelli, C., Banados, E., Decarli, R., et al. 2017a, ApJ, 834, 83
Mazzucchelli, C., Banados, E., Venemans, B., et al. 2017b, ApJ, 849, 91
McGreer, I., Fan, X., Strauss, M. A., et al. 2014, AJ, 148, 73M
Mechtley, M., Windshort, R. A., Ryan, R. E., et al. 2012, ApJL, 756, L38
Neeleman, M., Banados, E., Walter, F., et al. 2019, arXiv:1907.02536
Noeske, K. G., Weiner, B. J., Faber, S. M., et al. 2007, ApJL, 660, L43
Ota, K., Venemans, B., Taniguchi, Y., et al. 2018, ApJ, 856, 109
Ouchi, M., Shimasaku, K., Akiyama, M., et al. 2008, ApJS, 176, 301
Overzier, R. A., Guo, Q., Kauffmann, G., et al. 2009, MNRAS, 394, 577O
Peng, C. Y., Ho, L. C., Impey, C. R., & Rix, H.-W. 2002, AJ, 124, 266
Peng, C. Y., Ho, L. C., Impey, C. R., & Rix, H.-W. 2010, AJ, 139, 2097
Pentericci, L., Carniani, S., & Castellano, M. 2016, ApJL, 829, L11
Pogge, R. W., Atwood, B., Brewer, D. F., et al. 2010, Proc. SPIE, 7735, 9
Reed, S. L., Banerji, M., Becker, G. D., et al. 2019, MNRAS, 487, 1874
Reed, S. L., McMahon, R. G., Martini, P., et al. 2017, MNRAS, 468, 4702
Riechers, D. A., Bradford, C. M., Clemens, C. D., et al. 2013, Natur, 496, 329
Riechers, D. A., Carilli, C., Capak, P. L., et al. 2014, ApJ, 796, 84
Rodighiero, G., Daddi, E., Baronchelli, I., et al. 2011, ApJL, 739, L40
Salmon, B., Papovich, C., Finkelstein, S. L., et al. 2015, ApJ, 799, 183
Santini, P., Maiolino, R., Magnelli, B., et al. 2014, A&A, 563, A30
Sargsyan, L., Lebouteiller, V., Weedman, D., et al. 2012, ApJ, 755, 171
Scoville, N. Z., Evans, A. S., Dinshaw, N., et al. 1998, ApJL, 492, L107
Scoville, N. Z., Murchikova, L., Walter, F., et al. 2017, ApJ, 836, 66
Seifert, W., Appenzeller, I., Baumeister, H., et al. 2003, Proc. SPIE, 4841, 962
Selsing, J., Fynbp, J. P. U., Christensen, L., & Krogager, J.-K. 2016, A&A, 585, 87
Silva, L., Granato, G., Bressan, A., & Danese, L. 1998, ApJ, 509, 103
Simcoe, R. A., Burgasser, A. J., Bernstein, R. A., et al. 2008, Proc. SPIE, 7014, 70140
Somerville, R. S., Gilmore, R. C., Primack, J. R., & Dominguez, A. 2012, MNRAS, 423, 1992
Somerville, R. S., Hopkins, P. F., Cox, T. J., et al. 2008, MNRAS, 391, 481
Speagle, J. S., Steinhardt, C. L., Capak, P. L., & Silverman, J. D. 2014, ApJS, 214, 15
Spilker, J. S., Marrone, D. P., Aguirre, J. E., et al. 2014, ApJ, 785, 149
Steinhardt, C. L., Speagle, J. S., Capak, P., et al. 2014, ApJL, 791, L25
Straatman, C. M. S., Labbé, I., Spitler, L. R., et al. 2014, ApJ, 783L, 14
Toft, S., Smolcic, V., Magnelli, B., et al. 2014, ApJ, 782, 68
Trakhtenbrot, B., Paulina, L., Netzger, H., et al. 2017, ApJ, 836, 8
van Dokkum, P. G., Franx, M., Kriek, M., et al. 2008, ApJL, 677, L5
Venemans, B., McMahon, R. G., Walter, F., et al. 2012, ApJ, 751L, 25
Venemans, B. P., Decarli, R., Walter, F., et al. 2018, ApJ, 866, 159
Venemans, B. P., Verdoes Kleijn, G. A., Mwebaze, J., et al. 2015b, MNRAS, 453, 2259
Venemans, B. P., Walter, F., Decarli, R., et al. 2017, ApJ, 837, 146V
Venemans, B. P., Walter, F., Zschaechner, L., et al. 2016, ApJ, 816, 37V
Volonteri, M., & Rees, M. J. 2006, ApJ, 650, 669
Walter, F., Riechers, D., Cox, P., et al. 2009, Natur, 457, 699
Wang, F., Yang, Y., Fan, X., et al. 2018, arXiv:1810.11926
Wang, R., Wagg, J., Carilli, C., et al. 2013, ApJ, 773, 44
Weilbacher, P. M., Streicher, O., Urrutia, T., et al. 2012, Proc. SPIE, 8451E, 0B
Weilbacher, P. M., Streicher, O., Urrutia, T., et al. 2014, in ASP Conf. Ser. 485, Astronomical Data Analysis Software and Systems XXIII, ed. N. Manset & P. Forshay (San Francisco, CA: ASP), 451
Whitaker, K. E., Franx, M., Leja, J., et al. 2014, ApJ, 795, 104
Whitaker, K. E., Labbe, I., van Dokkum, P. G., et al. 2011, ApJ, 735, 86
Whitaker, K. E., Pope, A., Cybulski, R., et al. 2017, ApJ, 850, 208
Willott, C., Bergeron, J., & Omont, A. 2017, ApJ, 850, 108
Willott, C. J., Bergeron, J., & Omont, A. 2015, ApJ, 801, 123
Willott, C. J., Delorme, P., Reyle, C., et al. 2010, AJ, 139, 906
Wuyts, S., Cox, T. J., Hayward, C. C., et al. 2010, ApJ, 722, 1666
Yun, M. S., Ho, P. T. P., & Lo, K. Y. 1994, Natur, 372, 530
Zavala, J. A., Montana, A., Hughes, D. H., et al. 2018, NatAs, 2, 56